Trans. JSASS Space Tech. Japan
Vol. 7, No. ists26, pp. Pe_31-Pe_36, 2009

Operation Characteristics of Laser Driven Plasma Wind Tunnel

By Makoto MATSUI[1)], Koji SHINMI[1)], Tatsuya UENO[1)], Kimiya KOMURASAKI[2)] and Yoshihiro ARAKAWA[1)]

[1)]*Department of Aeronautics and Astronautics, The University of Tokyo, Tokyo, Japan*
[2)]*Department of Advanced Energy, The University of Tokyo, Chiba, Japan*

(Received April 25th, 2008)

A laser driven plasma wind tunnel using a 2 kW class continuous wave laser was developed as a high speed and high density atomic oxygen generator. Firstly, its operation conditions were examined. Using argon and oxygen as working gases, laser sustained plasma (LSP) was successfully produced in the plenum pressure range from 0.30 MPa to 0.95 MPa, and then the LSP was expanded to the vacuum chamber through the convergent-divergent nozzle. Next, plume characteristics were evaluated by Pitot probe and laser absorption spectroscopy using an absorption line of ArI 772.38 nm. As a result, the Mach number and the specific enthalpy around the center were 5.0 to 6.5 and 3.0 MJ/kg to 5.2 MJ/kg, respectively. The maximum flux density of atomic oxygen was estimated as 2.2×10^{21} $cm^{-2}s^{-1}$.

Key Words: High enthalpy flow, Laser plasma, Atomic oxygen, Laser absorption spectroscopy

Nomenclature

C_p	:specific heat at constant pressure
c	:velocity of light
d	:distance between LSP and throat
f	:flux density
h_0	:total specific enthalpy
h_{chem}	:chemical potential
I	:probe laser intensity
I_0	:incident probe laser intensity
K	:integrated absorption coefficient
k	:absorption coefficient
k_B	:Boltzmann constant
M	:Mach number
m	:mass of absorber
n	:number density
n_O	:number density of atomic oxygen
P	:CO_2 laser power
p_{amb}	:ambient pressure
p_{Pitot}	:Pitot pressure
p^*	:throat pressure
r	:radial position
R	:plume radius
T	:translational temperature
u	:flow velocity
x	:position in the laser path
y	:distance between the flow axis and the laser path
z	:distance from the nozzle exit
ν	:laser frequency
ν	:center absorption frequency
ν_{shift}	:Doppler shift
$\Delta\nu_D$	:Doppler width
θ	:incident laser beam angle to the flow
γ	:specific heat ratio

1. Introduction

Development of thermal protection systems (TPS) requires the simulation of entry and re-entry conditions at ground test facilities. Arc-heaters are widely used to generate such high enthalpy flows because of their long operational time, simple structure and ease of maintenance. [1–4)] However, surface catalytic effects and active and passive oxidation of TPS materials have been recognized as important issues [5–8)]; erosion of their electrodes poses an important obstacle because polluted flows make it difficult to evaluate chemical reaction rates in front of TPS surfaces.

Then, inductively coupled plasma (ICP) generators have garnered much attention. [9–12)] Such generators have no electrode. They can produce an ideal test condition for TPS tests because they have no undesirable chemical reactions that result from erosion. Another advantage of such generators is that they can use even reactive gases such as carbon dioxide and oxygen because of their electrode-less heating. However, in ICP, plasma instability limits its operation pressure less than atmosphere. Thereby, high enthalpy flows with high plenum pressure are difficult to produce. [13, 14)]

Therefore, laser sustained plasma (LSP) is one of alternative heating methods for high enthalpy flow generation. Since LSP is produced by focusing laser beam, it requires no-electrode and it is sustained even at the higher pressure than atmosphere. [15, 16)]

In this study, argon-oxygen LSP was produced by 2 kW class continuous wave laser and it was expanded through a convergent-divergent nozzle to generate supersonic atomic oxygen flows. Then, plume characteristics were evaluated by Pitot probe and laser absorption spectroscopy (LAS).

2. Laser Sustained Plasma Generator

2.1. Concept of LSP generator

A conceptual figure of the LSP generator is shown in Fig. 1. A laser beam is focused into a plasma production chamber through a set of condensing lens and window. Once plasma is produced near a focal point, the plasma efficiently absorbs a beamed laser power through inverse bremsstrahlung radiation. This plasma is sustained where its propagation to the incident laser beam direction balances out the flow velocity. The high-temperature LSP heats a working gas, and then the gas was expanded through a convergent-divergent nozzle to generate a high enthalpy flow.

In this generator, energy loss is composed of laser transmission and thermal losses. [17] The laser transmission is the unabsorbed laser power, which depends on the electron density and the volume of LSP. In thermal losses, the convective heat transfer to the chamber wall is usually small because the core of LSP does not attach directly to the wall and the cold flow surrounds the LSP. On the other hand, the radiative loss from the LSP increases with an increase in temperature of LSP. In this way, the energy efficiency of this generator depends on the energy balance in the energy transfer processes.

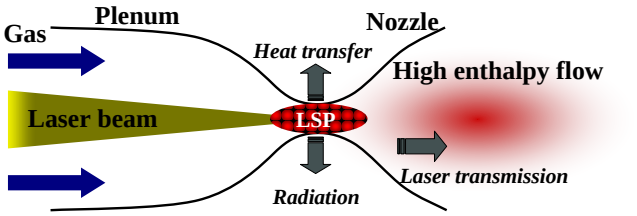

Fig. 1. Conceptual figure of LSP generator

2.2. Experimental setup of LSP generator

A schematic of the LSP generator is shown in Fig. 2. The generator is composed of a laser induction window, a plasma-sustaining channel, and a convergent-divergent nozzle. The throat diameter is 1.0 mm and nozzle diameter is 20 mm. The designed Mach number for argon flows is about 10, where for simplicity the specific heat ratio is fixed. [18, 19] As a beam source, a continuous wave carbon dioxide laser (YB-L200B7T4, Matsushita Electric Industrial Co., Ltd.) was used. The wavelength is 10.6 μm. The maximum output power is 2 kW and the transverse mode of the laser beam is TEM_{10}. The beam divergence is less than 2 mrad at the laser exit. The beam diameter of 20 mm was magnified by factor of 2.2 using a ZnSe beam expander, and the expanded beam was condensed into the generator through a ZnSe plano-convex lens. The focal length of the lens was 250 mm, corresponding to 7.4 in F-number which was defined as focal length normalized by beam diameter. This lens can move back to forth in the laser beam direction using a traverse stage.

A rod made of stainless steel (SUS304) was used as the source of the initial electron emission. After the ignition, the LSP was moved toward the nozzle throat by moving the focal lens position.

The generator is connected to a vacuum chamber. The chamber is 0.5 m in diameter and 1 m in length and it has two view windows enabling to diagnose an expanded flow. With two series of rotary vacuum pumps (ULVAC, VS1501;40 m^3/h) and mechanical booster pumps (ULVAC, PRC012A; 500 m^3/h), the ambient pressure can be kept under 106 Pa at the mass flow rate of argon 1.49 g/s.

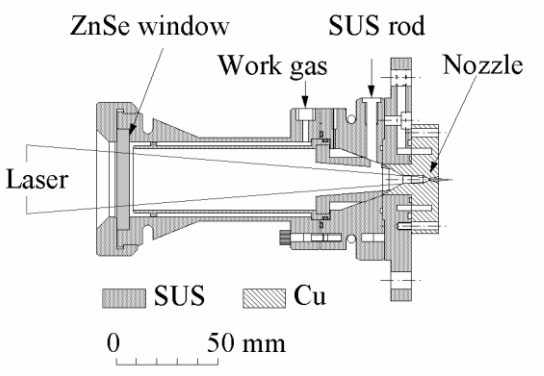

Fig. 2. Schematic of LSP generator

3. Measurement Methods

3.1. Pitot probe

Mach number is estimated from the ratio of the Pitot pressure to the ambient pressure by Rayleigh supersonic Pitot formula, expressed as

$$\frac{p_{\mathrm{Pitot}}}{p_{\mathrm{amb}}} = \left[\frac{(\gamma+1)M^2}{2}\right]^{\frac{\gamma}{\gamma-1}} \left[\frac{\gamma+1}{2\gamma M^2-(\gamma-1)}\right]^{\frac{1}{\gamma-1}}. \quad (1)$$

A schematic of the Pitot probe developed at the University of Tokyo was shown in Fig.3. The probe made of cupper has a bore diameter of 2 mm and a probe outer diameter of 6 mm along the first 30 mm in length, and then it is covered by double tube cooling system whose outer diameter is 12 mm in order to protect the probe tip from melting. Pitot pressure was measured by a diaphragm gauge whose resolution was 0.13 Pa (DIAVAC Limited, FTR-1 and F-133k). The measurement point was 10 mm downstream from the nozzle exit.

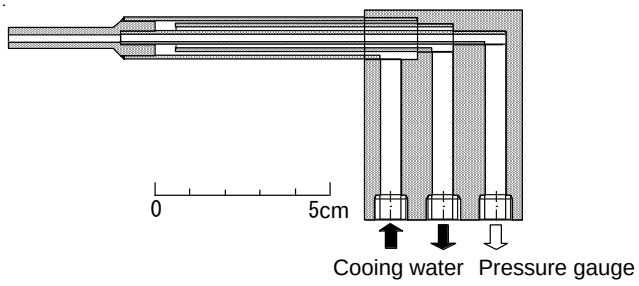

Fig. 3. Schematic of Pitot probe

3.2. Principle of laser absorption spectroscopy

The translational temperature and the flow velocity were measured by a diode laser based LAS system developed at the University of Tokyo. [3,4]

The relationship between laser intensity and absorption

coefficient is expressed by the Beer-Lambert law as

$$\frac{\mathrm{d}I(\nu,y)}{\mathrm{d}x} = -k(\nu,x,y)I(\nu,y). \quad (2)$$

Because the measured signals are composed of path-integrated absorption coefficient, the Abel inversion was applied to obtain the local absorption coefficient. When axisymmetric distributions of flow properties are assumed, the absorption coefficient in the radial coordinate is obtained as,

$$k(\nu,r) = \frac{1}{\pi}\int_r^R \frac{d\left\{\ln\left[(I/I_0(y,\nu))\right]\right\}/dy}{\sqrt{y^2-r^2}}dy. \quad (3)$$

The absorption coefficients are dependent on the frequency. Then the Abel inversion should be conducted frequency by frequency.

In our experimental conditions, Doppler broadening is several gigahertzes, which is two orders of magnitude greater than all other broadenings, including natural, pressure and Stark broadenings. The absorption profile is approximated as a Gaussian profile, expressed as

$$k(\nu,r) = \frac{2K(x)}{\Delta\nu_\mathrm{D}}\sqrt{\frac{\ln 2}{\pi}}\exp\left[-\ln 2\left\{\frac{2(\nu-\nu_0-\nu_\mathrm{shift})}{\Delta\nu_\mathrm{D}}\right\}^2\right]. \quad (4)$$

The Doppler width is the full width at half maximum of the profile and is related to the temperature, expressed as

$$\Delta\nu_\mathrm{D} = 2\nu_0\sqrt{\frac{2k_\mathrm{B}T}{mc^2}\ln 2}. \quad (5)$$

The shift of the center absorption frequency by Doppler effect is related to the flow velocity, expressed as

$$\nu_\mathrm{shift} = \frac{u\nu_0}{c}\sin\theta. \quad (6)$$

The target line is the absorption from argon meta-stable state at 772.38 nm.

3.3. LAS measurement system

Figure 4 shows a schematic of the measurement system. A tunable diode-laser with an external cavity (Velocity Model 6300, New Focus, Inc.) was used as the laser oscillator. Its line width was less than 500 kHz. The laser frequency was scanned over the absorption line shape. The modulation frequency and width were 1 Hz and 30 GHz, respectively. The laser intensity, which was normalized by saturation intensity, was reduced less than 10^{-2} by neutral density filters; it was sufficiently small to avoid the influence of absorption saturation. [20] An optical isolator was used to prevent the reflected laser beam from returning into the external cavity. An etalon was used to calibrate relative frequency. Its free spectral range was 0.75 GHz. An argon glow discharge plasma tube (argon: 80 Pa, 250V) was used as a stationary plasma source to calibrate the laser frequency.

The probe beam was guided to the chamber window through an optical fiber. The fiber output was mounted on a one-dimensional traverse stage to scan the flow in the radial direction. The probe beam diameter was 1 mm at the chamber center. To reduce plasma emission, transmitted laser intensity was measured by a photo detector (DET110/M, Thorlabs, Inc.) with a 2-mm pinhole and a band-pass filter whose full width at half maximum was 10 nm (FB770-10, Thorlabs, Inc.). A parabola mirror allowed scanning of the plume without synchronizing the detector position with the probe beam position. The signals were recorded using a digital oscilloscope with 16-bit resolution at the sampling rate of 10 kHz (DL1540; YOKOGAWA Co.). A measurement plane was 10 mm downstream from the nozzle exit and the incident laser beam angle was 5.0 degree.

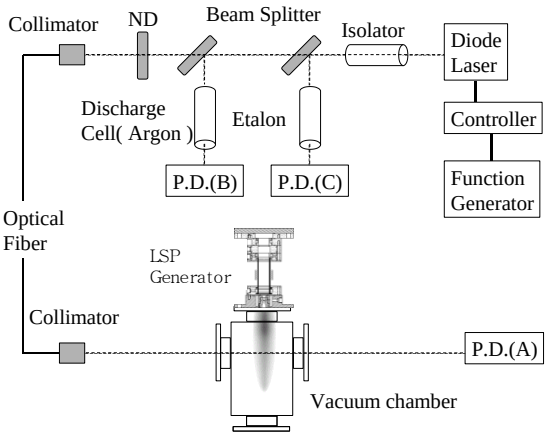

Fig. 4. LAS measurement system

4. Results and Discussion

4.1. Operation conditions

Operation conditions are tabulated in Table 1. The LSP could be produced in the plenum pressure range from 0.30 MPa to 0.95 MPa. It should be remarked that at the plenum pressure of 0.95 MPa, the ZnSe window of 4 mm thickness and 50 mm in diameter was broken during the test. Then in this paper, flow characterization was not evaluated at this condition. However, this does not mean the upper limit of the LSP production. The thicker window would enable to produce the LSP in the higher plenum pressure.

Figure 5 shows plume photos for the variation of the LSP position. Since the emission region of the plumes became larger with the closer position of the LSP to the nozzle throat, the LSP was optimized by moving a focal lens to maximize exhaust plume size. However, at the argon flow rate more than 1.19 g/s, the position was not optimized. In our previous research, the LSP was found to move upstream in the higher plenum pressure. [17] Then, the focal point should be set downstream from the throat in order to produce the LSP around the throat. However, the mechanical limit disabled the LSP to be set near the throat. Thereby, in these conditions, the focal lens was set to the closest position to the generator window.

The estimated thermal efficiency by measuring the increase in cooling water temperature was ranged from 37 % to 48 %.

Table 1. Operation conditions.

Properties	Value
Laser power, W	800
Argon, g/s	0.298-1.49 (1.93)
Oxygen, mg/s	2.38
Plenum pressure, MPa	0.30-0.74 (0.95)
Ambient pressure, Pa	43-106 (122)

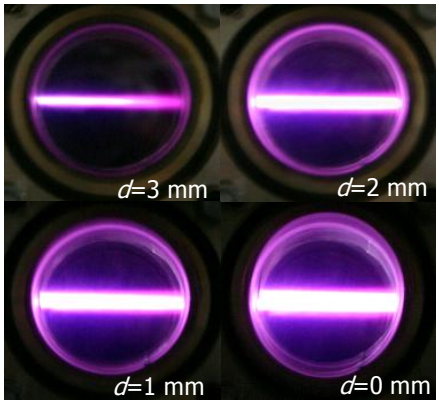

Fig. 5. Plume photos for the variation of LSP position (800W, Ar:0.595g/s)

4.2. Pitot measurement

Figure 6 shows the Pitot pressure and estimated Mach number using Eq. (1). The Pitot pressure increases with the increase in the argon flow rate and has a maximum of 4.0 kPa at the flow rate of 1.19 g/s. However, at the flow rate of 1.49 g/s, the Pitot pressure was still 4.0 kPa in spite of the higher plenum pressure. This might be because the LSP in this condition would be positioned upstream of the throat due to the unoptimized lens position and then the thermal loss to the wall increases.

Mach number has a maximum of 6.5 at the flow rate of 0.298 g/s and then decreases with the increase in the mass flow rate. This is because the increase in the plenum pressure caused by the increase in the temperature is more prominent at the lower mass flow rate, resulting in the higher pressure ratio.

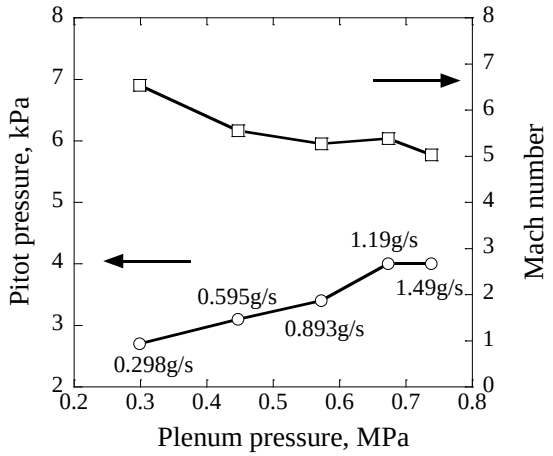

Fig. 6. Pitot pressure and estimated Mach number

4.3. LAS measurement

Figures 7 and 8 show a plume photo with the probe beam path and typical transmitted laser intensity and etalon signals, respectively. The transmitted laser intensity fluctuated. The fluctuation of 270 Hz agrees with that of plasma emission. This might be caused by the LSP oscillation due to the fluctuation of the laser power. [21] In this study, the maximum absorption values in each fluctuation were extracted and a Gasuss distribution was fitted to the envelope of the maximum absorption absorbance as shown in Fig.9.

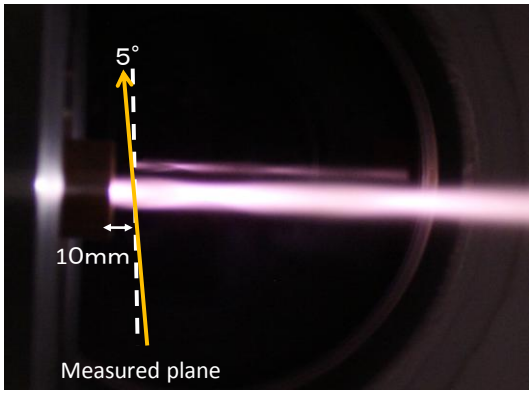

Fig. 7. Plume photo and measured plane (800W, Ar: 0.595g/s, O_2:2.38mg/s).

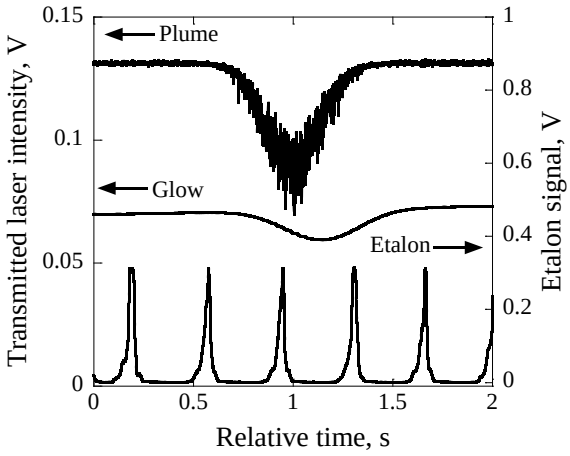

Fig. 8. Typical transmitted laser intensity and etalon signals

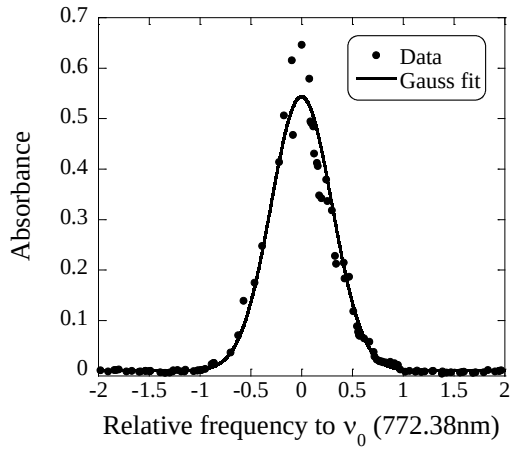

Fig. 9. Absorbance and Gauss fit

Figure 10 shows the deduced temperature distributions for various conditions. The temperature has almost flat distributions around 280 K to 350 K in the radial region less than 5 mm.

Figure 11 shows the flow velocity distributions. At the flow rate of 0.298 g/s and 0.893 g/s, the velocity has also flat distributions around 2650 m/s to 2890 m/s but its region is narrower than those of the temperature. At the flow rate of 1.49 g/s, the peak is located off-axis. In this

condition, due to the lowest input specific enthalpy, the pressure ratio is lower than those in the other conditions, which causes over-expansion, resulting in the flow separation in the nozzle. This might be because of the asymmetric velocity distribution.

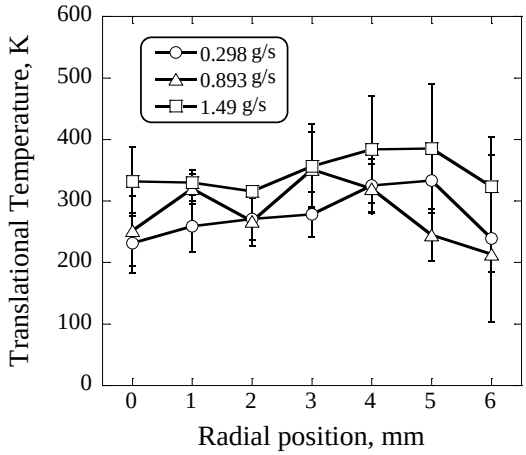

Fig. 10. Translational temperature distributions

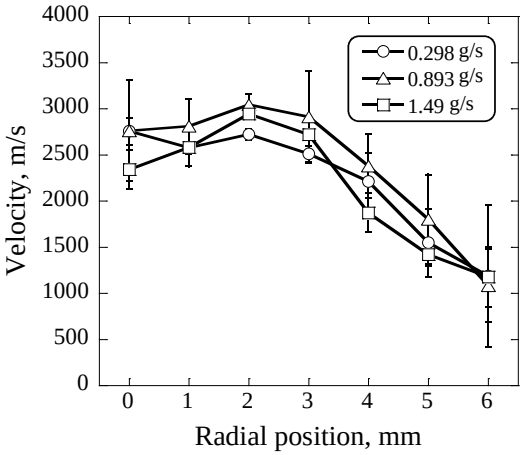

Fig. 11. Velocity distributions

4.4. Specific enthalpy and atomic oxygen flux density

The specific enthalpy and degree of dissociation in oxygen were estimated as follows. Assuming an isentropic expansion and chemically frozen flow through the nozzle, the total specific enthalpy is conserved expressed as

$$h = \begin{cases} \int_0^{T^*} C_p dT' + h_{\text{chem}} + \frac{1}{2}\gamma RT^* & \text{(Throat)} \\ \int_0^{T} C_p dT' + h_{\text{chem}} + \frac{1}{2}u^2 & \text{(Plume)} \end{cases} . \quad (7)$$

Here, the chemical potential is constant under the chemically frozen flow assumption.

Since the plenum pressure measured in the plenum chamber was higher than 0.20 MPa, the chemical composition at the throat was calculated assuming thermo-chemical equilibrium.

In the calculation, seven chemical species Ar, O_2, O, Ar^+, O_2^+, O^+ and e^-, and four chemical reactions $Ar \leftrightarrow Ar^+ + e^-$, $O_2 \leftrightarrow 2O$, $O \leftrightarrow O^+ + e^-$, $2O \leftrightarrow O_2^+ + e^-$ were considered. Their equilibrium constants were obtained from references 22 and 23. The volumetric gas mixture ratio argon and oxygen and the plenum pressure were set identical to the operation condition. The specific heat at the constant pressure was computed as the sum of the contributions of all species. Figure 12 shows typical calculated mole fraction and specific enthalpy as a function of the total temperature.

Using Eq. (7), the specific enthalpy and the degree of dissociation in oxygen were estimated. Figure 13 shows the estimated specific enthalpy distributions. The specific enthalpy at the flow rate of 0.298 g/s and 0.893 g/s has also flat region of 3.5 MJ/kg to 5.2 MJ/kg in the radial region less than 3 mm, where oxygen was found fully dissociated. The off-axis peak at the flow rate of 1.49 g/s is mainly because of the similar velocity distribution.

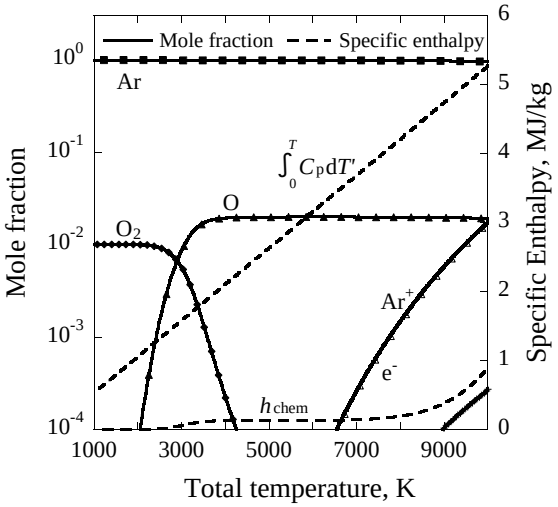

Fig. 12. Typical calculated specific enthalpy and mole fractions using the thermo-chemical equilibrium assumption, p^*=0.15 MPa, volumetric mixture ratio Ar: O_2=10:0.1

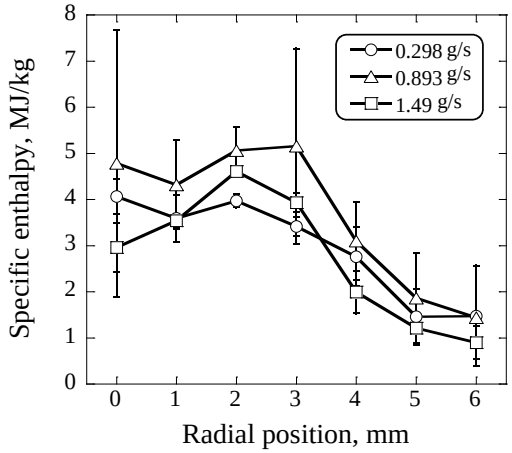

Fig. 13. Specific enthalpy distributions

The flux density of the atomic oxygen was estimated as

$$f = n_O u . \quad (8)$$

Here, the number density of atomic oxygen was estimated by the equation of state $p_{\text{amb}}=nk_BT$ and the calculated mole fraction. Figure 14 shows estimated flux density of the atomic oxygen on the axis as a function of the plenum pressure. The maximum flux density was 2.2×10^{21} $\text{cm}^{-2}\text{s}^{-1}$ at the plenum pressure of 0.30 MPa and then decreases

with the increase in the plenum pressure.

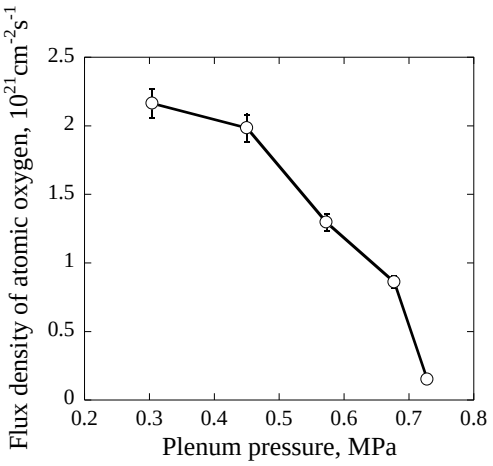

Fig. 14. Flux density of atomic oxygen on the axis as a function of plenum pressure

5. Conclusion

A laser driven plasma wind tunnel has been developed as a high speed and high density atomic oxygen generator. The flow characteristics were evaluated by Pitot probe and laser absorption spectroscopy. As a result, the Mach number and the specific enthalpy around the center were 5.0 to 6.5 and 3.0 MJ/kg to 5.2 MJ/kg with the plenum pressure of 0.30 MPa to 0.95 MPa, respectively. The maximum flux density of atomic oxygen was estimated as 2.2×10^{21} cm^{-2}s^{-1}.

Acknowledgments

This research was partially supported by the Ministry of Education, Science, Sports and Culture, Grant-in-Aid for Exploratory Research, 16656263 and Research Fellowships of the Japan Society for the Promotion of Science for Young Scientists 18-09885.

References

1) Birkan, M. A.: Arcjets and Arc Heaters: An Overview of Research Status and Needs, *J. Propulsion Power*, **12** (1996), pp. 1011–1017
2) Auweter-Kurtz, M., Kurtz, H. L., and Laure, S.: Plasma Generators for Re-Entry Simulation, *J. Propulsion Power*, **12** (1996), pp. 1053-1061.
3) Matsui, M., Takayanagi, H., Oda, Y., Komurasaki, K., and Arakawa, Y.: Performance of arcjet-type atomic-oxygen generator by laser absorption spectroscopy and CFD analysis, *Vacuum*, **73** (2004), pp. 341-346.
4) Matsui, M., Ikemoto, T., Takayanagi, H., Komurasaki, K., Arakawa, Y.,"Generation of Highly Dissociated Oxygen Flows Using a Constrictor-Type Arc Heater, *J. Thermophys. Heat. Tr.*, **21** (2007), pp.247–249.
5) Bykova, N. G., Vasil'evskii, S. A., Gordeev, A. N., Kolesnikov, A. F., Pershin, I. S., and Yakushin, M. I.: Determination of the Effective Probabilities of Catalytic Reactions on the Surfaces on Heat Shield Materials in Dissociated Carbon Dioxide Flows, *J. Fluid Dynamics*, **32** (1997), pp. 876-886.
6) Balat, M., Flamant, G., Male, G., and Pichelin, G..: Active to Passive Transition in the Oxidation of Silicon Carbide at High Temperature and Low Pressure in Molecular and Atomic Oxygen, *J. Materials Sci.*, **27** (1992), pp. 697-703.
7) Kisa, M., Li, L., Yang, J., Minton, T., Stratton, W. G., Voyles, P., Chen, X., Benthem, K., and Pennyycook, S. J.: Homogeneous Silica Formed by the Oxidation of Si(100) in Hyperthermal Atomic Oxygen, *J. Spacecraft Rockets*, **43** (2006), pp.431-435.
8) Fujimoto, L, Satoh, K., Shioya, T., Seki, N., and Fujita, K.: Degradation of Materials by High-Energy Atomic Oxygen, *JSME International J.* A, **46**, (2002), pp.283-289.
9) Herdrich, G., Auweter-Kurtz, M.: Development and Characterization of Inductively Heated Plasma Generator for Atmospheric Entry Simulations, *AIAA Paper 04-2503*, (2004).
10) Matsui, M, Komurasaki, K., Herdrich, G., and Auweter-Kurtz, M.: Enthalpy Measurement in Inductively Heated Plasma Generator Flow by Laser Absorption Spectroscopy, *AIAA J.* **43** (2005), pp. 2060-2064.
11) Matsui, M., Komurasaki, K., Arakawa, Y., Knapp, A., Herdrich, G., and Auweter-Kurtz, M.: Enthalpy Measurement of Inductively Heated Air Flow, *J. Spacecraft Rockets*, **45** (2008), pp.155-157
12) Ito, I., Ishida, K., Mizuno, M., Sumi, T., Fujita, K., Nagai, J., Murata, H. and Matsuzaki, T.: Heating Tests of TPS samples in 110kW ICP-heating wind tunnel, *ISTS* 2004-e-20
13) Yamada, T., Fujita, K., Nonaka, S., Ishii, N.: Performance Characteristics of the Inductively-Coupled High Enthalpy Flow Generator with CO2 Gas, *ISTS* 2006-e-19.
14) Bottin, B., Varbonaro, M., Van der Haegen, V., and Paris, S.: Predictedand Measured Capability of the VKI 1.2 MW Plasmatron Regarding Re-Entry Simulation, Aerothermodynamics for Space Vehicles, ESA SP-426, ESA, Paris, and European Space Research and Technology Centre, Noordwijk, The Netherlands, 1998, pp. 553–560.
15) Toyoda, K. Komurasaki, K., Arakawa, Y.: Continuous-wave laser thruster experiment, *Vacuum*, **59** (2000), pp.63-72.
16) Toyoda, K. Komurasaki, K., Arakawa, Y.: Thrust Performance of a CW Laser Thruster in Vacuum, *Vacuum*, **65** (2002) pp.383-388.
17) Inoue, T., Uehara, S., Komurasaki, K., Arakawa, Y.: Energy Conversion in a CW Laser Thurster, *J Jpn. Soci. Aeronaut. Space Sci.*, **54** (2006), pp.168-174.
18) Bartz, D. R.: An Approximate Solution of Compressible Turbulent Boundary Layer Development and Convective Heat Transfer in Convergent-Divergent Nozzles, *Trans. ASME*, **77** (1955), pp. 1235-1245.
19) Burm, K. T. A. L. , Goedheer, W. J. and Schram, D. C.: The isentropic exponent in plasmas, *Phys. Plasma*, 6 (1999), pp.2622-2627.
20) Matsui, M., Ogawa, S., Komurasaki, K., Arakawa, Y.: Influence of Laser Intensity on Absorption Line Broadening in Laser Absorption Spectroscopy, *J. Appl. Phys.*, **100** (2006), 063102.
21) Inoue, T., Ijiri, T., Hosoda, S., Kojima, K., Uehara, S., Komurasaki, K., Arakawa, Y.: Oscillation phenomenon of laser-sustained plasma in a CW laser propulsion, *Vacuum*, **73** (2004) pp.433-438.
22) Matsuzaki, R.: Quasi-One-Dimensional Aerodynamics with Chemnical Vibrational and Translational Nonequilibrium, *Trans. Jpn. Soc. Aeronaut. Space Sci.*, **30** (1987), pp. 243-258.
23) Guputa, R. N., Yos, J. M., Thompson, R. A., and Lee, K.-P.: A Review of Reaction Rates and Thermodynamic and Transport Properties for an 11-Species Air Model for Chemical and Thermal Nonequilibrium Calculations to 30000K, *NASA Reference Publication* 1232 (1990).